# Efficient technique for *ab-initio* calculation of magnetocrystalline anisotropy energy

Junfeng Qiao[a,b], Weisheng Zhao[a,b,*]

[a]*Fert Beijing Institute, BDBC, Beihang University, Beijing 100191, China*
[b]*School of Electronic and Information Engineering, Beihang University, Beijing 100191, China*

## Abstract

*Ab-initio* calculation of magnetocrystalline anisotropy energy (MCAE) often requires a strict convergence criterion and a dense $k$-point mesh to sample the Brillouin zone, making its convergence problematic and time-consuming. The force theorem for MCAE states that MCAE can be calculated by the band energy difference between two magnetization directions at a fixed potential. The maximally localized Wannier function can be utilized to construct a compact Hilbert space of low-lying electron states and interpolate band eigenvalues with high precession. We combine the force theorem and the Wannier interpolation of eigenvalues together to improve the efficiency of MCAE calculations with no loss of accuracy. We use a Fe chain, a Fe monolayer and a FeNi alloy as examples and demonstrate that the Wannier interpolation method for MCAE is able to reduce the computational cost significantly and remain accurate simultaneously, compared with a direct *ab-initio* calculation on a very dense $k$-point mesh. This efficient Wannier interpolation approach makes it possible for large-scale and high-throughput MCAE calculations, which could benefit the design of spintronics devices.

*Keywords:* magnetocrystalline anisotropy energy, *ab-initio*, Wannier function
*PACS:* 75.30.Gw, 71.15.-m, 85.75.-d

## 1. Introduction

In ferromagnetic (FM) materials, the magnetic anisotropy energy (MAE) is the difference between magnetizing energies along two directions. MAE can be mainly separated into the extrinsic part and the intrinsic part. The extrinsic shape anisotropy, in which MAE correlates with the shape of the FM material, originates from the magnetic dipole-dipole interaction [1, 2]. The intrinsic magnetocrystalline anisotropy energy (MCAE) arises from the collective effect

---

*Corresponding author
*Email address:* weisheng.zhao@buaa.edu.cn (Weisheng Zhao)

of the crystal structure and spin-orbit coupling (SOC). The orbital motions of electrons are restricted to specific orientations by the crystal field, and the SOC couples the spin degree of freedom and the orbital motion. Consequently, the energy of the crystal depends on the magnetization orientation [3].

Usually, the MCAE is on the order of meV at surfaces and interfaces [4, 5, 6], about 3 orders of magnitude larger than that of bulk crystals [7, 1]. Apart from the interest in fundamental science, the practical applications have also stimulated lots of research into the understanding and optimization of MCAE [8, 9, 10, 11, 12, 13]. One of the applications is the magnetic tunnel junction (MTJ), which is the core structure of magnetic random access memory (MRAM) [14, 15]. MTJ stores one bit of information by the relative magnetization orientation of the two FM layers, and the read process is based on tunneling magnetoresistance [16, 17, 18]. The large MCAE induced by the CoFe/MgO interface is crucial for the stability of the information.

The MCAE is hard to be captured because of its small magnitude. The total energy of a crystal unit cell is on the order of $1 \times 10^3$ eV, while the MCAE is on the order of $1 \times 10^{-3}$ eV, this significant contrast poses serious challenges not only to experimental instruments but also to numerical algorithms. As a result, calculation of MCAE still remains an intriguing problem in the *ab-initio* community [19, 1, 20, 21, 22].

In *ab-initio* calculations, plane wave (PW) algorithm is widely adopted because it is mathematically simple and in principle complete. The PW method provides the same accuracy at all points in space, this advantage on one side is appealing but on the other side is disappointing since it often requires large amounts of plane waves to converge and results in bad scaling behavior when system size increases. A more efficient approach is always desired. Maximally localized Wannier function (MLWF) is the Fourier transform of the reciprocal space PW wave function under the criterion of maximal localization of Wannier function (WF) in real space [23]. MLWF not only gives a clearer physical insight of chemical bondings but also manifests its necessities and accuracies in the calculations of many physical properties, such as electric polarization [24], anomalous hall conductivity [25] and orbital magnetization [26], etc. [23, 27, 28].

Here we extend the Wannier interpolation method to MCAE calculation for the purpose of improving efficiency. Our steps are summarized as follows: First, an *ab-initio* calculation is performed on a relatively coarse $k$-point mesh (kmesh). Second, MLWFs are extracted from the acquired *ab-initio* wave functions. Third, MCAE calculations are performed on a much denser kmesh in the Wannier representation. Compared to a direct *ab-initio* calculation on the dense kmesh, this Wannier interpolation approach has equivalent accuracy but greatly reduced computational cost. The initial coarse kmesh is too sparse for MCAE to converge but the extracted WFs meet the criterion of "good" localization. Our Wannier interpolation approach could not only reduce the computational cost but also make it possible to calculate MCAE for large systems requiring extremal computational resources, and calculations requiring exceptionally high accuracy.

## 2. Methods

The Wannier interpolation method for calculating MCAE is based on two theories: The force theorem (FT) states that MCAE can be calculated by the difference between band energies of two magnetization directions; the MLWF provides an efficient way for interpolating eigenvalues on arbitrary dense kmesh based on coarse kmesh *ab-initio* calculation. We first give a brief and self-contained introduction to the Wannier interpolation of band structure, then show our procedures for combining Wannier interpolation with the FT of MCAE. We followed the theory and mathematical notations used in Yates *et al.* Ref.[29] and Marzari *et al.* Ref.[23]. The disentanglement of entangled bands is omitted for conciseness and detailed theory on MLWFs can be found in Ref.[29] and Ref.[23].

### 2.1. Wannier interpolation

#### 2.1.1. Construction of WFs

In a periodic crystal, the Bloch theorem allows us to write down the wave function as

$$\psi_{n\boldsymbol{k}}(\boldsymbol{r}) = e^{i\boldsymbol{k}\boldsymbol{r}} u_{n\boldsymbol{k}}(\boldsymbol{r}), \tag{1}$$

where $\boldsymbol{k}$ is the k-point vector, $n$ is the band index, $\psi_{n\boldsymbol{k}}(\boldsymbol{r})$ is the Bloch wave function, $u_{n\boldsymbol{k}}(\boldsymbol{r})$ is periodic in real space. Inserting Bloch function into the Kohn-Sham equation, we arrive at the equation for the periodic part of the Bloch function,

$$\hat{H}(\boldsymbol{k})u(\boldsymbol{k}) = \epsilon_{\boldsymbol{k}} u(\boldsymbol{k}), \tag{2}$$

where $\hat{H}(\boldsymbol{k})$ is the transformed Hamiltonian $\hat{H}(\boldsymbol{k}) = e^{-i\boldsymbol{k}\boldsymbol{r}} \hat{H} e^{i\boldsymbol{k}\boldsymbol{r}}$, $\epsilon_{\boldsymbol{k}}$ is the eigenvalue. Usually one needs several thousand plane waves to expand the $u(\boldsymbol{k})$ in the PW method and the diagonalizations of the Hamiltonian matrices having the rank of several thousand are performed on each k-point. This is why a direct *ab-initio* calculation on a dense kmesh is rather time-consuming.

Generally, Fourier transform enables us to have a different representation of functions in reciprocal space, and this may be useful for analysis of the problem, e.g. the frequency spectrum of audio signals and images. If treated properly, the reciprocal space should be equivalent to the original space, i.e. they are equivalent Hilbert spaces. We apply the Fourier transform to the Bloch wave function $\psi_{n\boldsymbol{k}}(\boldsymbol{r})$ which lies in the Brillouin Zone (BZ),

$$|\boldsymbol{R}n\rangle = \frac{V}{(2\pi)^3} \int_{\mathrm{BZ}} d\boldsymbol{k} e^{-i\boldsymbol{k}\cdot\boldsymbol{R}} |\psi_{n\boldsymbol{k}}\rangle, \tag{3}$$

thus $|\boldsymbol{R}n\rangle$ form an orthonormal set and span the same Hilbert space as $\psi_{n\boldsymbol{k}}(\boldsymbol{r})$. In principle, a smooth function in real space results in a localized function in its reciprocal space, and vice versa. It is not naturally guaranteed that the simply summed Bloch function of Equ. (3) results in a smooth function $|\boldsymbol{R}n\rangle$ in real space. Fortunate enough, there is a gauge freedom left in the definition of Bloch function,

$$|\tilde{\psi}_{n\boldsymbol{k}}\rangle = e^{i\varphi_n(\boldsymbol{k})} |\psi_{n\boldsymbol{k}}\rangle, \tag{4}$$

or equivalently,

$$|\tilde{u}_{n\boldsymbol{k}}\rangle = e^{i\varphi_n(\boldsymbol{k})}|u_{n\boldsymbol{k}}\rangle. \tag{5}$$

We can utilize this freedom to construct localized WFs in real space, the so-called maximally localized Wannier function.

We define the unitary transformation which takes the original Bloch function $|u_{n\boldsymbol{k}}\rangle$ to the smoothed function $|\tilde{u}_{n\boldsymbol{k}}\rangle$ (from now on written as $|u_{n\boldsymbol{q}}^{(W)}\rangle$, we use $\boldsymbol{q}$ here as to differentiate another kmesh in the following Wannier interpolation step) as

$$|u_{n\boldsymbol{q}}^{(W)}\rangle = \sum_{m=1}^{M} |u_{m\boldsymbol{q}}\rangle\mathcal{U}_{mn}(\boldsymbol{q}), \tag{6}$$

where $M$ is the number of states needs to be considered for our targeted physical properties, usually the low-lying states below Fermi energy or plus few empty states above. We call this unitary transformation as the transformation from Bloch gauge to Wannier gauge.

Thus, the Fourier transform pair between the smoothed Bloch functions and the MLWFs are

$$|\boldsymbol{R}n\rangle = \frac{1}{N} \sum_{\boldsymbol{q}} e^{-i\boldsymbol{q}\cdot\boldsymbol{R}}|u_{n\boldsymbol{q}}^{(W)}\rangle,$$

$$\Updownarrow \tag{7}$$

$$|u_{n\boldsymbol{q}}^{(W)}\rangle = \sum_{\boldsymbol{R}} e^{i\boldsymbol{q}\cdot\boldsymbol{R}}|\boldsymbol{R}n\rangle,$$

where, $N$ is the number of points in BZ.

*2.1.2. Interpolation on arbitrary kmesh*

For the reciprocal space Hamiltonian operator $\hat{\boldsymbol{H}}(\boldsymbol{q})$, we define the $M \times M$ Hamiltonian matrix in the Wannier gauge as

$$H_{nm}^{(W)}(\boldsymbol{q}) = \langle u_{n\boldsymbol{q}}^{(W)}|\hat{\boldsymbol{H}}(\boldsymbol{q})|u_{m\boldsymbol{q}}^{(W)}\rangle = [\mathcal{U}^{\dagger}(\boldsymbol{q})H(\boldsymbol{q})\mathcal{U}(\boldsymbol{q})]_{nm}, \tag{8}$$

where $H_{nm}(\boldsymbol{q}) = \mathcal{E}_{n\boldsymbol{q}}\delta_{nm}$, $\delta_{nm}$ is the Kronecker delta function. If the $H_{nm}^{(W)}(\boldsymbol{q})$ is diagonalized by

$$U(\boldsymbol{q})^{\dagger}H^{(W)}(\boldsymbol{q})U(\boldsymbol{q}) = H^{(H)}(\boldsymbol{q}), \tag{9}$$

where $H_{nm}^{(H)}(\boldsymbol{q}) = \mathcal{E}_{n\boldsymbol{q}}^{(H)}\delta_{nm}$, then $\mathcal{E}_{n\boldsymbol{q}}^{(H)}$ will be identical to the original *ab-initio* $\mathcal{E}_{n\boldsymbol{q}}$.

Transforming the Hamiltonian operator from reciprocal space to real space,

$$H_{nm}^{(W)}(\boldsymbol{R}) = \frac{1}{N} \sum_{\boldsymbol{q}} e^{-i\boldsymbol{q}\cdot\boldsymbol{R}}H_{nm}^{(W)}(\boldsymbol{q}), \tag{10}$$

and then performing inverse Fourier transform

$$H_{nm}^{(W)}(\boldsymbol{k}) = \sum_{\boldsymbol{R}} e^{i\boldsymbol{k}\cdot\boldsymbol{R}}H_{nm}^{(W)}(\boldsymbol{R}), \tag{11}$$

4

we succeed in interpolating the Hamiltonian operator on arbitrary $k$-point $\boldsymbol{k}$. Since the WFs we have chosen are maximally localized, the $H_{nm}^{(W)}(\boldsymbol{R})$ is expected to be exponentially localized in real space, a few $\boldsymbol{R}$ are sufficient in the sum of Equ. (11).

The final step is diagonalizing $H_{nm}^{(W)}(\boldsymbol{k})$,

$$U(\boldsymbol{k})^{\dagger} H^{(W)}(\boldsymbol{k}) U(\boldsymbol{k}) = H^{(H)}(\boldsymbol{k}), \tag{12}$$

then the acquired eigenvalues on arbitrary $k$-point $\boldsymbol{k}$ can be used for later extractions of the targeted physical properties. We comment here that since $H^{(W)}(\boldsymbol{k})$ are of dimensions $M \times M$, their diagonalizations are very "cheap", compared with the diagonalizations of the Hamiltonian matrices in PW method, which are on the order of more than $1000 \times 1000$ dimensions.

Figure 1 shows the interpolated band structure of our later used Fe chain compared with the original coarse kmesh *ab-initio* calculation and a dense kmesh *ab-initio* calculation. The calculation details will be described in section 3.1. The interpolated band structure is in excellent agreement with the dense kmesh *ab-initio* band, whether it locates at the coarse kmesh *ab-initio* $\boldsymbol{q}$-points or the interpolated $\boldsymbol{k}$-points between the $\boldsymbol{q}$-points. Apparently, the coarse kmesh *ab-initio* calculation, from which the WFs are constructed, is far from convergence with respect to the dense kmesh *ab-initio* calculation.

### 2.2. MCAE

As mentioned in the introduction, one of the difficulties of calculating MCAE is its small magnitude compared with the total energy. Another difficulty is its rapid variation in $k$-space. As shown in Fig. 2(b), the $k$-space resolved MCAE, defined by Equ. (14), displays sharp peaks and steps along $k_z$ direction. To capture these tiny but critical features, a sufficiently dense kmesh must be adopted, and slow convergences relative to kmesh are often the case in the calculations of MCAE.

In the *ab-initio* calculation of MCAE, the most natural and rigorous method is performing two self-consistent (SCF) calculations of different magnetization directions, and the MCAE should be the difference between the total energies. Written down by notations, the MCAE between two crystallographic directions can be defined as

$$\text{MCAE} = E^{90^{\circ}} - E^{0^{\circ}}, \tag{13}$$

where $E^{\alpha}$ is the total energy of magnetization pointing towards the $\theta = \alpha$ direction, $\theta$ is the spherical polar angle with respect to the crystallographic $\boldsymbol{c}$ axis. In our case, we choose $\alpha = 90^{\circ}$ and $0^{\circ}$, and the azimuthal angle $\phi$ is kept fixed to 0 in all the calculations. According to this definition, MCAE $> 0$ stands for perpendicular magnetic anisotropy (PMA) while MCAE $< 0$ stands for in-plane magnetic anisotropy (IMA).

However, the cumbersome diagonalizations are rather time-consuming, especially when SOC is included, and reaching the energy minimal becomes much harder in the SCF iterations. According to the FT [7, 20, 1, 30, 31, 32], the
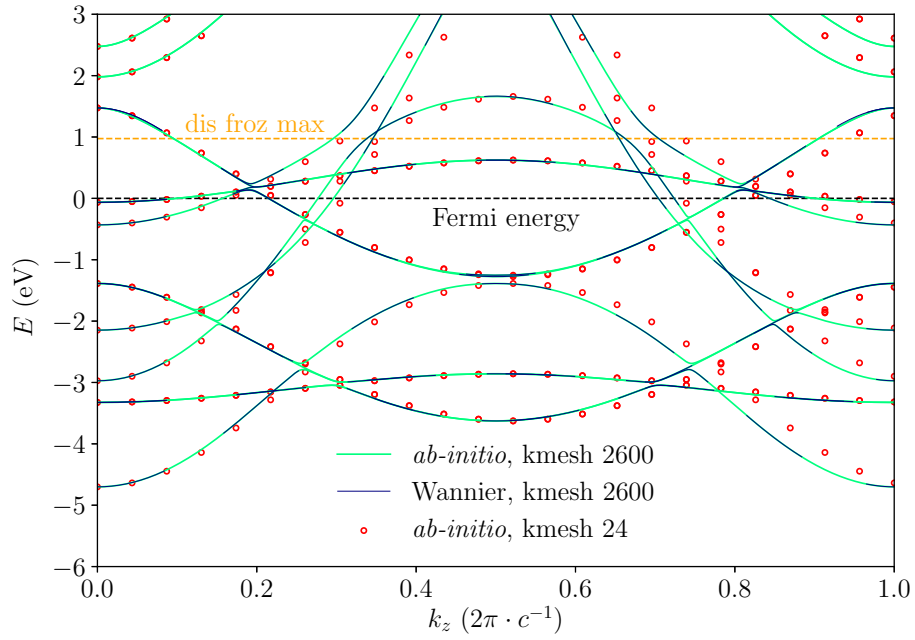
Figure 1: Comparison of Fe chain band structures obtained from a coarse kmesh $1 \times 1 \times 24$ *ab-initio* calculation (red circles), a dense kmesh $1 \times 1 \times 2600$ *ab-initio* calculation (green lines), and the interpolated band structure on the dense kmesh $1 \times 1 \times 2600$ by MLWFs (blue dashed lines). The MLWFs are constructed from the coarse kmesh $1 \times 1 \times 24$ *ab-initio* calculation. The black dashed horizontal line corresponds to the Fermi energy, the orange dashed horizontal line corresponds to the upper limit of the frozen inner window in the disentanglement process when constructing MLWFs. The $k$-points on the horizontal axis are along the crystallographic $\boldsymbol{c}$ axis and are in fractional coordinates.

main contribution to the MCAE originates from the difference of band energies between two magnetization directions at fixed potential,

$$\text{MCAE}(\boldsymbol{k}) = \sum_i f_{i\boldsymbol{k}}^{90°} \epsilon_{i\boldsymbol{k}}^{90°} - \sum_{i'} f_{i'\boldsymbol{k}}^{0°} \epsilon_{i'\boldsymbol{k}}^{0°},$$

$$\text{MCAE} = \frac{1}{N} \sum_{\boldsymbol{k}} \text{MCAE}(\boldsymbol{k}), \tag{14}$$

where $\boldsymbol{k}$ is the $k$-point vector, $i$ and $i'$ are the band indexes of magnetization directions along $\theta = 90°$ and $\theta = 0°$, respectively. $f_{i\boldsymbol{k}}$ is occupation number and $\epsilon_{i\boldsymbol{k}}$ is the energy of band $i$ at $k$-point $\boldsymbol{k}$, $N$ is the number of $k$-points in the BZ.

Thus by non-self-consistent (NSCF) calculation of only a one-step diagonalization, the eigenvalues are obtained and the MCAE can be calculated by Equ. (14). The FT is widely adopted and its validity has been proved by practical calculations [33, 34, 22]. Good matches between experimental and *ab-initio* results are also found in the literature [35, 36]. Another merit of FT is that by Equ. (14) some $k$-space resolved analyses can be performed, such as the contribution of the quantum well states to the oscillation of MCAE [10].

The practical calculation of MCAE involves two steps. First, charge density is acquired self-consistently without taking into account SOC. Second, reading the SCF charge density, two NSCF calculations are performed including SOC, with magnetization pointing towards the $\theta = 90°$ and the $\theta = 0°$ directions, respectively. Finally, MCAE is calculated via Equ. (14).

Before we finish the discussion of FT for MCAE, we would like to emphasize the importance of Fermi energy $E_F$. Since MCAE is such a small quantity that is on the order of meV, a small displacement of $E_F$ will propagate into the occupation numbers $f_{i\boldsymbol{k}}$, and then the MCAE by Equ. (14). The MCAE will be significantly modified, even the sign could be changed. To accurately calculate MCAE, the small difference of Fermi energy between magnetizations along $\theta = 90°$ and $\theta = 0°$ must be considered. Since the number of electrons $N_{elec}$ are the same between two magnetization directions, the Fermi energies are calculated separately for $\theta = 90°$ and $\theta = 0°$ in the Wannier interpolation steps by

$$N_{elec} = \int^{E_F^{90°}} n^{90°}(E)dE = \int^{E_F^{0°}} n^{0°}(E)dE, \tag{15}$$

where $E_F^{\alpha}$ and $n^{\alpha}(E)$ are the Fermi energy and density of states for magnetization along $\theta = \alpha$, $\alpha = 90°$ or $0°$. Also, the occupation numbers $f_{i\boldsymbol{k}}$ are calculated separately for the two magnetization directions. Finally, MCAE is calculated by Equ. (14).

In all, Wannier interpolation gives us the ability to efficiently interpolate band energies on arbitrary kmesh, the FT tells us the MCAE can be calculated by the difference of band energies. Combining these two theories together, MCAE calculations can be carried out on a much denser kmesh with no loss of accuracy but greatly reduced computational cost.

We implemented the code for MCAE calculations on the basis of Wannier90 package [37, 38, 39, 40]. In the next section, we choose a Fe chain

as an example to demonstrate our method of MCAE calculation and discuss some convergence issues in the calculations. On one hand, due to the lowered crystal symmetry, the Fe chain system is expected to have medium magnitude MCAE; on the other hand, this system is small enough that an extremely dense kmesh *ab-initio* calculation can be performed so that our Wannier interpolation method can be directly compared with high accuracy *ab-initio* results. After discussing all the critical convergence issues in the Wannier interpolation approach, we further carry out MCAE calculations of Fe monolayer, which has MCAE on the order of sub meV and the results can be validated against literature. Finally, the MCAE of bulk materials are on the order of $\mu$eV and their *ab-initio* calculations are very challenging, we show that even in such a tough situation as FeNi alloy, our Wannier interpolation approach still faithfully recover the converged MCAE from a coarse kmesh calculation, and the results well match other *ab-initio* calculations and experiments. The three examples are respectively 1-dimension, 2-dimensions, and 3-dimensions, with MCAE varying from meV to $\mu$eV. Their convergence criteria are increasingly tighter, and their densities of kmesh increase linearly, quadratically and cubically when testing the MCAE convergence. These examples are good test grounds for verifying Wannier interpolation approach of MCAE.

## 3. Fe chain

### *3.1. ab-initio calculation and Wannierization*

The *ab-initio* calculations were performed using the QUANTUM ESPRESSO (QE) package based on the projector-augmented wave (PAW) method and a plane wave basis set [41, 42]. The exchange and correlation terms were described using generalized gradient approximation (GGA) in the scheme of Perdew-Burke-Ernzerhof (PBE) parameterization, as implemented in the PSLIBRARY version 0.3.1 [43]. We used a wave function cutoff of 90 Ry and electron density cutoff of 1080 Ry. A Marzari-Vanderbilt cold smearing [44] of width 0.002 eV was adopted. Convergence relative to smearing width and kmesh will be detailedly discussed in the subsequent paragraph. Since the MCAE of the Fe chain is on the order of meV, the energy convergence criteria of all the calculations were set as $1.0 \times 10^{-8}$ Ry. We kept a 15 Å vacuum space in the xy plane to eliminate interactions between periodic images. Since enough vacuum space was left in the xy plane, we set the Monkhorst-Pack $k$-point mesh to $1 \times 1 \times 24$ and confirmed that increasing it to $2 \times 2 \times 24$ or more had negligible impacts on MCAE. The unit cell contains one Fe atom [shown in Fig. 2(a)] and the lattice constant along $\boldsymbol{c}$ axis (i.e. the atomic spacing along the Fe chain) was set as 2.2546 Å, which was acquired by relaxation until the force acting on the Fe atom was less than $1 \times 10^{-2}$ Ry/Bohr.

To transform Bloch functions into MLWFs, first, the overlap matrices $M_{mn}^{\boldsymbol{k},\boldsymbol{b}}$ and the projection matrices $A_{mn}^{\boldsymbol{k}}$ are extracted from the Bloch functions [23]. Then after disentanglement and Wannierization the MLWFs are constructed. We used 20 spinor WFs having the form of $sp3d2$, $dxy$, $dxz$, $dyz$, and $s$-like Gaussians. The disentanglement outer energy window was set as $[-100.0, 10.0]$eV,
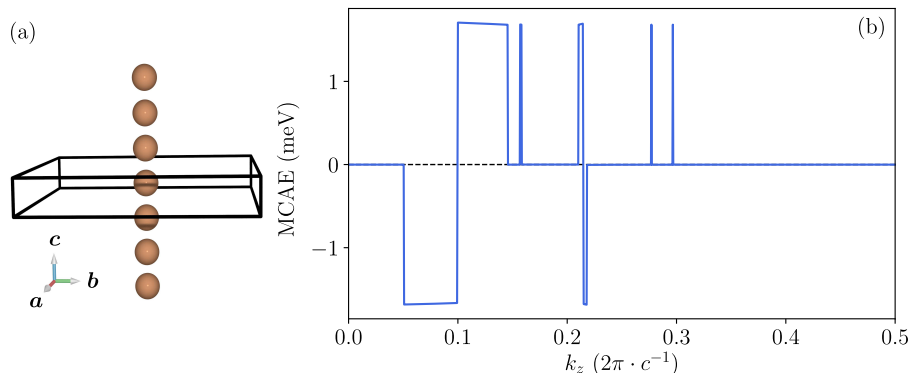
Figure 2: (a) Crystal structure of the Fe chain. The chain is along the crystallographic $c$ axis. The cuboid represents the unit cell. (b) $k$-resolved Fe chain MCAE along $k_z$ axis, defined by Equ. (14). Only half of the $k$-space is shown.

and the inner window was set as $[-100.0, -3.41]$eV, which is slightly higher than the Fermi energy $-4.38$ eV. The spreads of WFs signify the quality of localization, as defined by [23]

$$\Omega = \sum_n [\langle \mathbf{0}n|r^2|\mathbf{0}n\rangle - \langle \mathbf{0}n|\mathbf{r}|\mathbf{0}n\rangle^2], \tag{16}$$

where $|\mathbf{0}n\rangle$ are the WFs in the home unit cell. The convergence threshold of spread for both the disentanglement and Wannierization were set as $1 \times 10^{-10}$ Å$^2$. Apart from 2 WFs having the spread $\Omega$ around $2.0$ Å$^2$, the spreads of the remaining 18 WFs were smaller than $1.0$ Å$^2$, mostly around $0.2$ Å$^2$. The total spread of WFs was around $10.0$ Å$^2$ and the convergence issues will be discussed in the next section.

### 3.2. Convergence issues of Wannier interpolation

Three main parameters should be tested to reach a reliable result of MCAE: the number of coarse *ab-initio* kmesh $n_k^{ab}$ for the construction of MLWFs, the number of Wannier interpolation kmesh $n_k^{wan}$ for the interpolation of MCAE from MLWFs, and the smearing width $\sigma$ that determines the fictitious smearing contributions to the total energies.

Note since the kmesh in the xy plane is always set as $1 \times 1$, we will use the number of $k$-points along z-axis $n_k$ as the shorthand of the kmesh $1 \times 1 \times n_k$. We differentiate the coarse *ab-initio* kmesh and the dense Wannier interpolation kmesh by the notation $n_k^{ab}$ and $n_k^{wan}$.

To make a clearer separation among different tests, we obey the notation that for a function $f(x; y)$, the $x$ before the semicolon is the variable while the $y$ after the semicolon is the parameter which is held fixed. For example, $\mathrm{MCAE}(n_k^{ab}; n_k^{wan})$ represents the variation of MCAE relative to the coarse *ab-initio* kmesh $n_k^{ab}$ when the Wannier interpolation kmesh $n_k^{wan}$ is held fixed.

9

Next, we test the convergence of the spread relative to the number of coarse *ab-initio* kmesh $\Omega(n_k^{ab})$, the convergence of MCAE relative to the the the number of coarse *ab-initio* kmesh $\text{MCAE}(n_k^{ab}; n_k^{wan}, \sigma)$, the convergence of MCAE relative to the number of Wannier interpolation kmesh $\text{MCAE}(n_k^{wan}; n_k^{ab}, \sigma)$, the convergence of MCAE relative to the smearing width $\text{MCAE}(\sigma; n_k^{ab}, n_k^{wan})$ and the minimum number of Wannier interpolation kmesh needed relative to smearing width $n_k^{wan}(\sigma)$.

Before carrying out quantitative analyses, we introduce several definitions to avoid ambiguities.

1. The *convergence indicator* $\delta f(x)$ of a function $f(x)$ is defined as

$$\delta f(x) = |\max_{y \geq x} f(y) - \min_{y \geq x} f(y)|, \tag{17}$$

   where $|\ldots|$ means taking the absolute value.
2. Let $\epsilon$ be a positive real number, we say that the function $f(x)$ is *converged at $x_0$ under the threshold $\epsilon$* if $\delta f(x) < \epsilon$ is satisfied for any $x \geq x_0$.
3. The *converged value $\bar{f}$* is defined as

$$\bar{f} = \sum_{\{x | \delta f(x) < \epsilon\}} f(x), \tag{18}$$

   i.e. if $f(x)$ is converged at $x_0$, then $\bar{f} = \sum_{x \geq x_0} f(x)$.
4. The *deviation* of a function $f(x)$ is defined as

$$\Delta f(x) = f(x) - \bar{f} \tag{19}$$

*3.2.1. Spread of WFs*

The construction of WFs relies on a uniform *ab-initio* kmesh, we call it as coarse *ab-initio* kmesh, since this kmesh does not need to be dense enough for the MCAE to be converged but is sufficient once "good" localization of WFs are reached.

Here we show the relation of WFs' spread and the density of *ab-initio* kmesh in Fig. 3(a). In the MCAE calculations, the "good" criterion for the localization of WFs is ultimately determined by the convergence of the MCAE. We mention it in advance that a $1 \times 1 \times 2600$ interpolation kmesh and a smearing width of $0.0012\,\text{eV}$ are sufficient for MCAE to be converged on the order of $1 \times 10^{-6}\,\text{eV}$, and the converged MCAE is $2.358 \pm 0.001\text{meV}$ with Fe magnetic moment parallel to the chain. The subsequent paragraphs will detailedly discuss the convergence issues related to interpolation kmesh and smearing width. We use this conclusion here to exclude the influence of the Wannier interpolation kmesh and the smearing width when discussing the convergence of the WFs' spread and the MCAE relative to the density of the *ab-initio* kmesh.

We use the indicator $\delta\Omega(n_k^{ab})$ to represent the convergence trend of the spread $\Omega$ calculated on *ab-initio* kmesh $n_k^{ab}$

$$\delta\Omega(n_k^{ab}) = |\max_{i \geq n_k^{ab}} \Omega(i) - \min_{i \geq n_k^{ab}} \Omega(i)|. \tag{20}$$

10

As shown in the inset of Fig. 3(a), when $n_k^{ab} \geq 24$, the $\delta\Omega$ are less than $0.2\,\text{Å}^2$. We use $\Delta\text{MCAE}(n_k^{ab})$ to represent the deviation of $\text{MCAE}(n_k^{ab})$ relative to the converged $\overline{\text{MCAE}}$. In this case, they are defined as

$$\Delta\text{MCAE}(n_k^{ab}) = \text{MCAE}(n_k^{ab}) - \overline{\text{MCAE}},$$

$$\overline{\text{MCAE}} = \frac{1}{9} \sum_{n_k^{ab}=22}^{30} \text{MCAE}(n_k^{ab}), \tag{21}$$

where $n_k^{ab}$ is the *ab-initio* kmesh used for the construction of WFs, $\overline{\text{MCAE}}$ is the mean value of MCAE calculated with *ab-initio* kmesh from 22 to 30 and these are the converged value since the variation between these 9 values are on the order of $1 \times 10^{-6}\,\text{eV}$, as shown in the inset of Fig. 3(b).

An interesting anomaly appears in the inset of Fig. 3(b) at $n_k^{ab} = 21$. This may be caused by the insufficiencies of coarse *ab-initio* kmesh or the Wannier interpolation kmesh. To separate the influence of these two kmeshes, we show the convergence indicator $\delta\text{MCAE}(n_k^{wan}; n_k^{ab})$ by the red error bar in the inset of Fig. 3(b). The $\delta\text{MCAE}(n_k^{wan}; n_k^{ab})$ is defined as

$$\delta\text{MCAE}(n_k^{wan}; n_k^{ab}) = |\max_{i \geq n_k^{wan}} \text{MCAE}(i; n_k^{ab}) - \min_{i \geq n_k^{wan}} \text{MCAE}(i; n_k^{ab})|, \tag{22}$$

where $n_k^{wan}$ is in the range of 2500 to 2700. At each specific $n_k^{ab}$, $\delta\text{MCAE}(n_k^{wan}; n_k^{ab})$ only varies less than $3 \times 10^{-6}\,\text{eV}$ when $n_k^{wan}$ changes from 2500 to 2700, much smaller than the anomaly. This indicates that the fixed Wannier interpolation kmesh of $n_k^{wan} = 2600$ is high enough and the anomaly at $n_k^{ab} = 21$ is caused by the *ab-initio* kmesh alone. This means to get a very accurate MCAE, a sufficiently dense *ab-initio* kmesh is needed for constructing high-quality MLWFs. However, compared with the *ab-initio* kmesh $n_k^{ab} = 2600$ used for a direct *ab-initio* computation of MCAE, this kmesh is much sparser and only use $0.8\,\%$ of the number of $k$-points.

For $n_k^{ab} \geq 22$, the total spread of WFs converges to approximately $0.2\,\text{Å}^2$, at the same time the MCAE converge on the order of $1 \times 10^{-6}\,\text{eV}$ as shown in the inset of Fig. 3(b). As in many other cases, the interpolated band structure agrees very well with high-density kmesh *ab-initio* calculation [23]. While the band structure of the coarse *ab-initio* kmesh, which is used for the construction of MLWFs, deviates largely from the "true" dense kmesh band structure needed for MCAE to converge. The comparison of band structures is shown in Fig. 1.

### 3.2.2. Interpolation kmesh

The former paragraphs consider the convergence of MCAE with respect to *ab-initio* kmesh, which should be dense enough for constructing MLWFs. From now on, we fix the $n_k^{ab}$ to 24. Once high-quality MLWFs are constructed, the next step for reaching converged MCAE is the Wannier interpolation. This is where the computational cost is significantly reduced.
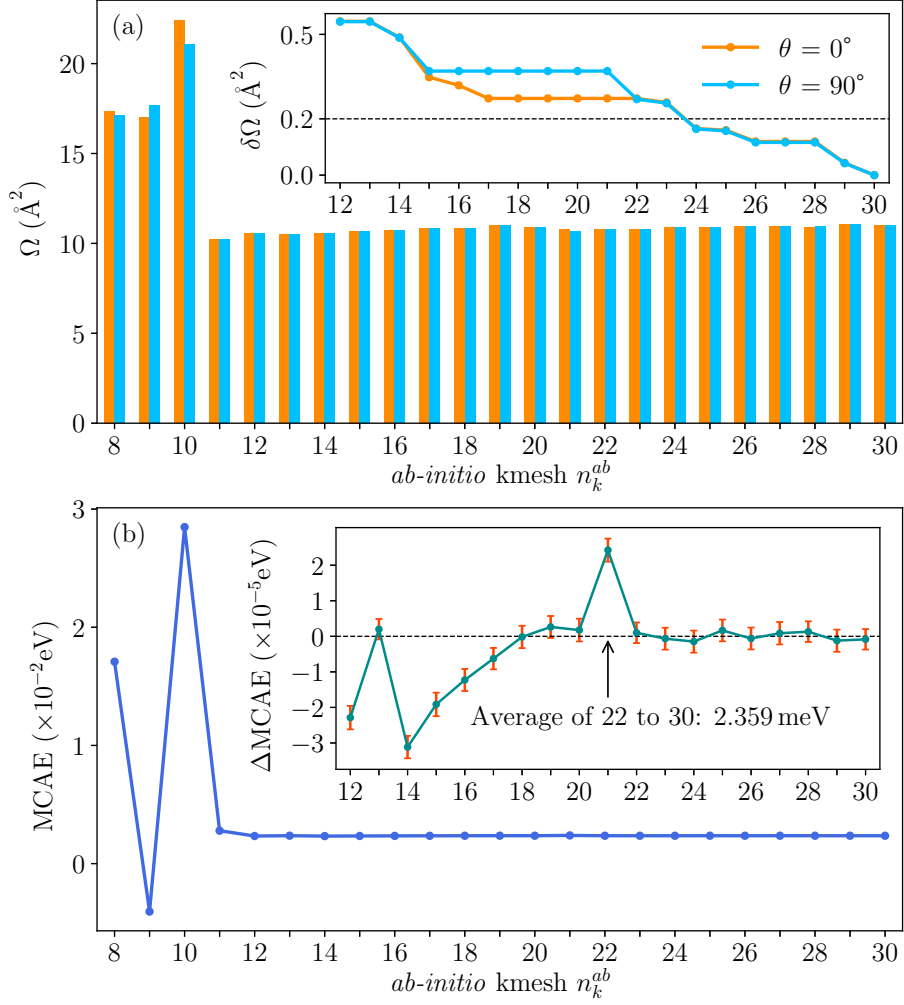
Figure 3: For Fe chain: (a) Spread of WFs relative to the density of *ab-initio* kmesh, the inset shows the convergence trend $\delta\Omega(n_k^{ab})$ of the spread defined by Equ. (20). Blue color and orange color are the calculations of magnetization direction perpendicular to and along the Fe chain, respectively. (b) The MCAE relative to the density of *ab-initio* kmesh. The inset shows the deviation of MCAE when approaching convergence, defined by Equ. (21). The red error bars in the inset represent the convergence trend $\delta\text{MCAE}(n_k^{wan}; n_k^{ab})$ relative to $n_k^{wan}$ as defined by Equ. (22). The small error bars indicate that the anomaly at $n_k^{ab} = 21$ is caused by the *ab-initio* kmesh alone and this means *ab-initio* kmesh plays a critical role in Wannier interpolation of MCAE.
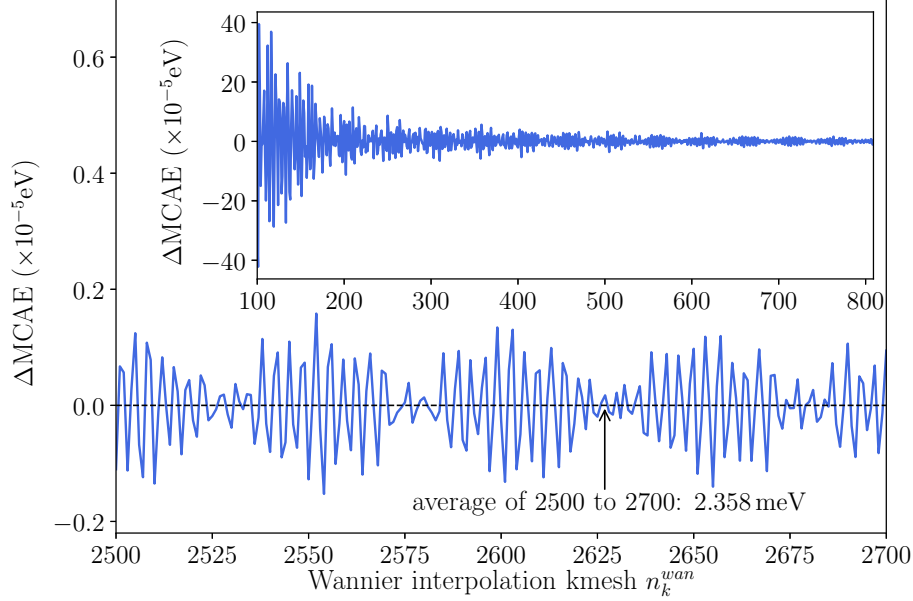
Figure 4: The Fe chain MCAE deviation relative to the converged value when Wannier interpolation kmesh $n_k^{wan}$ varies, defined by Equ. (23). The inset is the overview with $n_k^{wan}$ from 100 to 800.

In such circumstance, the $\Delta$MCAE is defined as

$$\Delta\text{MCAE}(n_k^{wan}) = \text{MCAE}(n_k^{wan}) - \overline{\text{MCAE}},$$
$$\overline{\text{MCAE}} = \frac{1}{201} \sum_{n_k^{wan}=2500}^{2700} \text{MCAE}(n_k^{wan}), \tag{23}$$

and this is shown in Fig. 4.

The inset of Fig. 4 shows the overview of the $\Delta$MCAE($n_k^{wan}$) for $n_k^{wan}$ from 100 to 800. Apparently, $n_k^{wan}$ on the order of 100 is far from convergence. For $n_k^{wan}$ around 2600, the MCAE converge under $4 \times 10^{-6}$ eV.

### 3.2.3. Smearing contribution

Smearing is very important for the convergence of *ab-initio* calculations. Large smearing is beneficial for fast convergence, but this may introduce a fictitious and un-negligible contribution to the total energy. Too small smearing may slow down the convergence significantly, and often one needs a much denser kmesh to converge. This problem can be largely alleviated because the Wannier interpolation is very "cheap"—as we mentioned in the Sec.2 it only involves diagonalizations of $M \times M$ matrices. One could easily increase kmesh density and reduce smearing width, or even not resorting to smearing.

The relation between the minimum number of interpolation kmesh $n_k^{wan}$ and the smearing width $\sigma$ is shown in the inset of Fig. 5 and the specific values are tabulated in Table 1. When $\sigma$ is in the range of $0.20\,\mathrm{eV}$ to $0.05\,\mathrm{eV}$, only less than 300 $n_k^{wan}$ is needed to converge the MCAE on the order of $2 \times 10^{-6}\,\mathrm{eV}$. However, as indicated by the blue line in the inset of Fig. 5, the smearing contribution to the MCAE, $\Delta\mathrm{MCAE}(\sigma; n_k^{wan})$, is on the order of $2 \times 10^{-3}\,\mathrm{eV}$, leading to unreliable results. $\Delta\mathrm{MCAE}(\sigma; n_k^{wan})$ is defined as

$$\Delta\mathrm{MCAE}(\sigma; n_k^{wan}) = \mathrm{MCAE}(\sigma; n_k^{wan}) - \overline{\mathrm{MCAE}},$$
$$\overline{\mathrm{MCAE}} = \frac{1}{10} \sum_{\sigma \in \Sigma} \mathrm{MCAE}(\sigma; n_k^{wan}), \text{where } \Sigma = \{0.0001 \times i | 0 \leq i \leq 9\}, \quad (24)$$

where the $n_k^{wan}$ are fixed to 2600, and the 0.0000 in $\Sigma$ means calculation without smearing.

We find a smearing width of less than $0.003\,\mathrm{eV}$ is able to reduce the smearing contribution to under $2 \times 10^{-6}\,\mathrm{eV}$, and at such a minimal smearing width a kmesh of nearly 1600 should be adopted. To totally exclude the smearing contribution, i.e. calculation without smearing, a dense kmesh of 2600 should be used [data listed in Table 1].

Finally, as the best touchstone for the validity of Wannier interpolation, we performed an extremely accurate *ab-initio* calculation, with a kmesh of $1 \times 1 \times 2600$ and a smearing width of $0.0010\,\mathrm{eV}$. As shown in Table 1, considering the numerical accuracy of $0.001\,\mathrm{meV}$, the Wannier interpolation results of rows No.9 to 11 are exactly equal to the dense kmesh *ab-initio* result of row No.15. The MLWFs used for interpolating MCAEs in rows No.1 to 11 are constructed from the *ab-initio* calculation of row No.13. It is clear from rows No.12 to 14 that the *ab-initio* calculation of row No.13 is not converged but the constructed MLWFs successfully recover the "true" MCAE.

### 3.3. Computational resources

So far we have demonstrated that our Wannier interpolation approach for calculating MCAE is sufficiently accurate. To illustrate its effectiveness in relieving the computational cost, we directly compare the resources used in the different calculations.

The computational resources and time spent for each calculation are shown in Table 2. All of the *ab-initio* results are calculated on 96 CPU cores. The *ab-initio* calculation on kmesh 2600 took $9.0\,\mathrm{h}$, while *ab-initio* calculation on kmesh 24 took several minutes. Note the most time-consuming step in the Wannier interpolation method—the disentanglement and Wannierization processes—can be boosted by selecting better initial projection orbitals. In the current work, we do not further investigate the choice of initial projection orbitals and we expect a better choice can greatly reduce the time spent on disentanglement and Wannierization. The biggest advantage of the Wannier interpolation method is that once the MLWFs are constructed, interpolations on kmesh of arbitrary density can be performed with negligible time. Apart from the computational

Table 1: The Fe chain MCAE and the minimum Wannier interpolation kmesh needed for convergence with respect to smearing width $\sigma$. The data in this table are plotted in the inset of Fig. 5. The MCAEs in rows of No.12 to 15 are directly calculated by QE, as indicated by QE in the Notes column. While the MCAEs in rows of No.1 to 11 are calculated by Wannier interpolation, as indicated by Wan in the Notes column. The $\sigma = 0.0000$ in the row No.11 represents calculation without smearing. The MLWFs used for interpolating MCAEs in rows No.1 to 11 are constructed from the *ab-initio* calculation of row No.13.

| No. | $\sigma$ (eV) | $n_k^{ab}$ | MCAE (meV) | min $n_k^{wan}$ | Notes |
|-----|---------|--------|------------|-----------|-------|
| 1   | 0.2000  | 24     | 3.678 62   | 72        | Wan   |
| 2   | 0.1700  | 24     | 4.298 54   | 81        | Wan   |
| 3   | 0.1500  | 24     | 4.698 43   | 93        | Wan   |
| 4   | 0.1300  | 24     | 5.039 60   | 113       | Wan   |
| 5   | 0.1000  | 24     | 5.144 34   | 158       | Wan   |
| 6   | 0.0700  | 24     | 3.857 64   | 225       | Wan   |
| 7   | 0.0500  | 24     | 2.121 76   | 319       | Wan   |
| 8   | 0.0200  | 24     | 2.115 46   | 725       | Wan   |
| 9   | 0.0030  | 24     | 2.358 76   | 1575      | Wan   |
| 10  | 0.0012  | 24     | 2.358 21   | 2670      | Wan   |
| 11  | 0.0000  | 24     | 2.357 39   | 2598      | Wan   |
| 12  | 0.0272  | 23     | 3.262 19   | None      | QE    |
| 13  | 0.0272  | 24     | 1.766 03   | None      | QE    |
| 14  | 0.0272  | 25     | 1.239 16   | None      | QE    |
| 15  | 0.0010  | 2600   | 2.358 67   | None      | QE    |
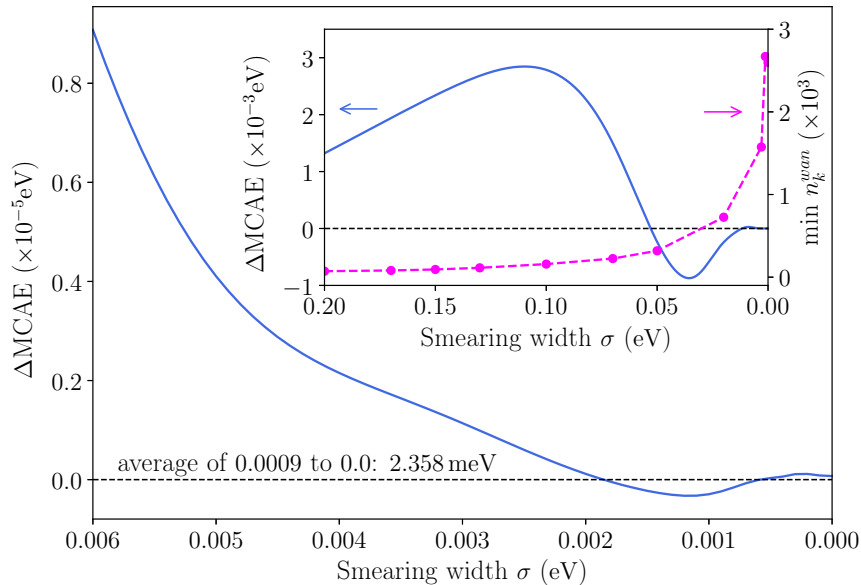
Figure 5: Fe chain MCAE convergence relative to smearing width $\sigma$, defined by Equ. (24). The inset is the overview for $\sigma$ from 0.20 eV to 0.00 eV. The magenta line in the inset is the minimum number of Wannier interpolation kmesh $n_k^{wan}$ needed for each smearing width $\sigma$.

time being saved, the computational resources needed for the interpolation is rather small, only 1 CPU core is sufficient for interpolation on arbitrary kmesh. If simply use

$$\text{Cost} = \text{CPU cores} \times \text{Wall time}, \tag{25}$$

as an estimation of computational cost, the direct *ab-initio* calculation costs $864 \, \text{hour} \cdot \text{core}$, the total cost of the Wannier interpolation method is $18 \, \text{hour} \cdot \text{core}$, i.e. we achieved a 48 times speedup.

We comment here that the adaptive refinement of kmesh and the adaptive smearing algorithms frequently used in MLWF interpolation of other physical properties [29, 23] are not necessary since it is already enough convenient to interpolate MCAE on arbitrary dense kmesh. For MCAE calculations, smearing should be avoided and the main concern is the quality of MLWFs. Once high-quality MLWFs are constructed, the following interpolation can be easily performed with very high accuracy and negligible cost.

## 4. Fe monolayer

The prototypical calculations on Fe chain have demonstrated the effectiveness of Wannier interpolation and we have discussed several convergence issues when employing Wannier interpolation to calculate MCAE. In this section, we perform calculations on Fe monolayer, which can be directly validated against

16

Table 2: Computational resources spent by direct dense kmesh *ab-initio* calculation and by Wannier interpolation method in the MCAE calculations of Fe chain. The cost is defined by Equ. (25). The Time in the third column is the wall time, and they are the sum of calculations for two magnetization directions. The unit of Cost is hour·core and is the sum of all the calculation steps. The Time = 0 in the last row means the time spent was less than a second, negligible.

| Calculations | CPU cores | Time | Cost |
|---|---|---|---|
| direct *ab-initio*, kmesh 2600 | 96 | 9.0 h | 864 |
| Wannier interpolation | | | |
|    a. coarse *ab-initio*, kmesh 24 | 96 | 5.8 min | |
|    b. projections & overlaps | 96 | 3.8 min | 18 |
|    c. disentanglement & Wannierization | 1 | 2.5 h | |
|    d. interpolation, kmesh 2600 | 1 | 0 | |

former results in the literature. In the next section we will show calculations on FeNi alloy, which can be compared with many *ab-initio* calculations and experimentally measured values.

The MCAE of Fe monolayer was calculated as 0.7 meV based on ultrasoft pseudopotential (USPP) result [31]. To make a direct comparison, we used the same structure as in Ref.[31], i.e. (001) Fe monolayer with lattice constant 2.85 Å and 8 Å vacuum separation in the z-direction. The *ab-initio* calculations were performed using QE based on PAW-GGA. We used a wave function cutoff of 60 Ry and an electron density cutoff of 500 Ry. A Methfessel-Paxton smearing of width 0.05 eV was adopted. To accurately determine MCAE, a kmesh of $50 \times 50 \times 1$ was used in the SCF calculation.

As is shown in Fig.6(a), for a direct *ab-initio* calculation, a kmesh higher than $62 \times 62 \times 1$ is needed to converge MCAE under 0.05 meV, and the converged value of 0.48±0.05meV (magnetic moment perpendicular to the plane) is similar to that of 0.70meV in Ref.[31]. The 0.20 meV difference between our results and the Ref.[31] may be caused by different type of pseudopotentials.

Then we constructed MLWF from coarse kmesh *ab-initio* calculations and it was found that a kmesh of dimension $11 \times 11 \times 1$ was enough for the convergence of MCAE when using Wannier interpolation. The results of the convergence tests are compiled in Table 3. Apparently, from Fig.6(a) we can conclude that *ab-initio* calculations of kmesh around $11 \times 11 \times 1$ are far from convergence, but from Table 3 rows No.4 to 6, the $11 \times 11 \times 1$ kmesh *ab-initio* calculation is sufficient for the Wannier interpolation of MCAE. With the help of MLWF, equivalent accuracy MCAE value can be extracted from a calculation with only 3% the number of $k$-points needed for the converged *ab-initio* calculation. The accuracy of Wannier interpolation is even more convincing when comparing Fig.6(a) and (b). Two curves are nearly identical, i.e. the MCAE is faithfully recovered for each kmesh on the horizontal axis.

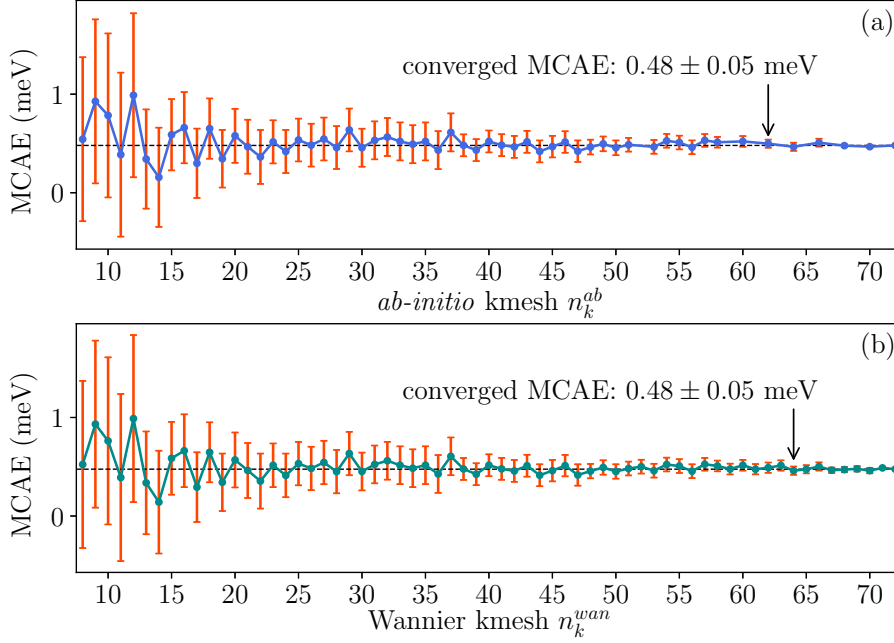As has been shown in Fig.5 and Table 1, smearing can be used to inhibit

17

Figure 6: Fe monolayer MCAE convergence relative to (a) *ab-initio* kmesh $n_k^{ab}$, and (b) Wannier interpolation kmesh $n_k^{wan}$. The MLWFs were constructed from *ab-initio* kmesh $11 \times 11 \times 1$, and it is clear from (a) that this kmesh is far from convergence if evaluating MCAE by direct *ab-initio* calculation. In fact, a kmesh of $62 \times 62 \times 1$ is needed for the *ab-initio* calculation to converge. The error bars are the convergence indicators obeying the definition of Equ.(17). To save computational time, we selectively calculated some of the kmeshes when $n_k^{ab} > 60$ in (a).

MCAE fluctuation and greatly reduce the density of kmesh needed for the convergence. However, the fictitious smearing will give rise to deviations around converged MCAE. In such circumstance, the Wannier interpolation is very helpful because we can cheaply increase the density of kmesh without resorting to smearing. We calculated the MCAE of Fe monolayer with different smearing width [Table 3 rows No.7 to 9] and it was found that kmesh should increase to more than $86 \times 86 \times 1$ to converge the MCAE. Since we have already used a small smearing width of $0.05\,\text{eV}$ in the *ab-initio* calculation, the MCAE hardly changes when reducing the smearing width. One noticeable irregularity is that the kmesh for convergence decreases when smearing width decreases. We speculate that this is caused by small numerical noises rather than a general trend.

In all, for the MCAE on the order of sub meV, the Wannier interpolation successfully recovers high accuracy *ab-initio* results from coarse kmesh *ab-initio* calculations.

18

Table 3: The convergence of Fe monolayer MCAE with respect to the *ab-initio* kmesh $n_k^{ab}$, Wannier interpolation kmesh $n_k^{wan}$ and smearing width $\sigma$. The MCAEs in rows of No.1 to 3 are directly calculated by QE, while the MCAEs in rows of No.4 to 9 are calculated by Wannier interpolation. The No.10 row is the result of USPP-GGA calculation from Ref.[31]. The number $n_k$ in columns 2 and 3 stands for kmesh $n_k \times n_k \times 1$.

| No. | $n_k^{ab}$ | $n_k^{wan}$ | $\sigma$ (eV) | MCAE (meV) | Notes |
|-----|------------|-------------|---------------|------------|-------|
| 1 | 10 | None | 0.05 | 0.78 | QE |
| 2 | 11 | None | 0.05 | 0.39 | QE |
| 3 | $\geq$62 | None | 0.05 | $0.48 \pm 0.05$ | QE |
| 4 | 10 | $\geq$74 | 0.05 | $0.67 \pm 0.05$ | Wan |
| 5 | 11 | $\geq$64 | 0.05 | $0.48 \pm 0.05$ | Wan |
| 6 | 12 | $\geq$64 | 0.05 | $0.47 \pm 0.05$ | Wan |
| 7 | 11 | $\geq$109 | 0.02 | $0.50 \pm 0.05$ | Wan |
| 8 | 11 | $\geq$99 | 0.01 | $0.50 \pm 0.05$ | Wan |
| 9 | 11 | $\geq$86 | 0.00 | $0.50 \pm 0.05$ | Wan |
| 10 | 40 | None | 0.05 | 0.70 | USPP[31] |

## 5. FeNi alloy

MCAE tends to be larger when symmetry is lower, and the MCAE of surfaces and interfaces are on the order of meV. Our calculations on Fe chain and Fe monolayer have validated that Wannier interpolation is capable of efficiently reducing the computational costs for MCAE in the region of meV. The calculation of bulk MCAE is much harder since their MCAE are usually on the order of $\mu$eV. What is even worse is that in 3 dimensions we need to sample the BZ along 3 directions, this means the number of $k$-points will increase cubically when we densify the kmesh for the convergence of MCAE. To further demonstrate the usefulness of Wannier interpolation, we performed calculations on FeNi alloy since a practical comparison between our Wannier interpolation results and other *ab-initio* calculations as well as experimental results can be made. Also, as a demonstration of the versatility of Wannier interpolation, we use GPAW[45, 46] as the *ab-initio* calculator in this subsection, since the construction of MLWF is irrelevant with the kind of the underlying *ab-initio* code and the Wannier interpolation approach is a post-processing tool capable of cooperating with different *ab-initio* calculator seamlessly.

Based on *ab-initio* calculations and experimental measurements, the MCAE of FeNi alloy is in the range of $0.48\,\text{MJ/m}^3$ to $0.77\,\text{MJ/m}^3$ [47, 48, 49, 50]. We used the same structure as in Ref.[49, 48], i.e. $L1_0$ FeNi with in-plane lattice constant $a = 3.56$Å and out-of-plane lattice constant $c = 3.58$Å. The calculated cell is $45°$ rotated relative to the conventional cell and the in-plane lattice constant is $a/\sqrt{2}$. The *ab-initio* calculations were performed using GPAW based on PAW-GGA with $600\,\text{eV}$ wave function cutoff and a Fermi-Dirac smearing of width $0.1\,\text{eV}$. A kmesh of $25 \times 25 \times 17$ was used in the SCF calculation and the convergence criterion was set as $1 \times 10^{-6}\,\text{eV}$.

For the *ab-initio* calculation, a kmesh of dimension $19 \times 19 \times 13$ is needed to converge MCAE [Fig.7 and Table 4 rows No.1 to 3]. The converged MCAE is $52\,\mu\text{eV}$ (magnetic moment along [001] axis), i.e. $0.37\,\text{MJ/m}^3$, a bit smaller than the value in the literature around $0.5\,\text{MJ/m}^3$ [47, 48, 49, 50]. Next, we construct MLWF based on coarse kmesh *ab-initio* calculations. It was found that kmesh of dimension $12 \times 12 \times 8$ is sufficient for constructing MLWFs and a kmesh of $21 \times 21 \times 21$ is enough for Wannier interpolation. Due to the limitations of GPAW-Wannier90 interface, the quality of the constructed MLWFs was not so good as that of QE. Nevertheless, the Wannier interpolated MCAE of $0.41 \pm 0.05\text{MJ/m}^3$ [Table 4 row No.6], still successfully recovered high density kmesh *ab-initio* result of $0.37 \pm 0.05\text{MJ/m}^3$ [Table 4 row No.3]. In this case, MLWFs enable us to get equivalent accuracy MCAE result from coarse kmesh of $25\,\%$ the number of $k$-points relative to the dense kmesh *ab-initio* calculation. We expect that by improving the GPAW-Wannier90 interface, the density of the $12 \times 12 \times 8$ kmesh for constructing MLWFs can be further reduced, thus higher efficiency when using Wannier interpolation.

In the *ab-initio* calculations we used a large smearing width of $0.1\,\text{eV}$, next we utilize Wannier interpolation to recover the MCAE without smearing. Upon decreasing smearing width to 0, a Wannier interpolation kmesh of dimension $67 \times 67 \times 67$ is needed to converge MCAE [Table 4 row No.7] and the result of $0.52 \pm 0.05\text{MJ/m}^3$ is quite similar to the literature. A $67 \times 67 \times 67$ kmesh means that the number of $k$-points is on the order of $300\,000$, such a large number of $k$-points poses serious challenges to *ab-initio* calculations. However, since in MLWF space the number of WFs is on the order of 10 to 100, the diagonalization of the Hamiltonian matrix is much cheaper thus the eigenvalues are efficiently computed. The Wannier interpolation is very helpful when it requires an extremely dense kmesh, and the case of FeNi alloy has proven that Wannier interpolation is capable of computing even bulk magnetocrystalline anisotropy energy.

## 6. Conclusions

We combine the Wannier interpolation of eigenvalues and the force theorem of magnetocrystalline anisotropy energy together to develop an efficient and accurate method for calculating MCAE. First, coarse kmesh *ab-initio* calculations are performed for different magnetization directions. Second, maximally localized Wannier functions are constructed based on the overlap matrices and projection matrices obtained from the first step. Third, MCAE is calculated based on FT and Wannier interpolation of eigenvalues on a dense kmesh. This Wannier interpolation method serves as a post-processing step for economically calculating MCAE other than brute-force *ab-initio* calculation. The ultimate accuracy of the calculated MCAE is determined by the underlying *ab-initio* code (the choice of exchange-correlation functionals, type of basis sets, etc.), since it is the *ab-initio* code that produces the Bloch functions from which the MLWFs are constructed. Nevertheless, the Wannier interpolation is independent of the choice of the underlying code, since the only quantities needed from the code are
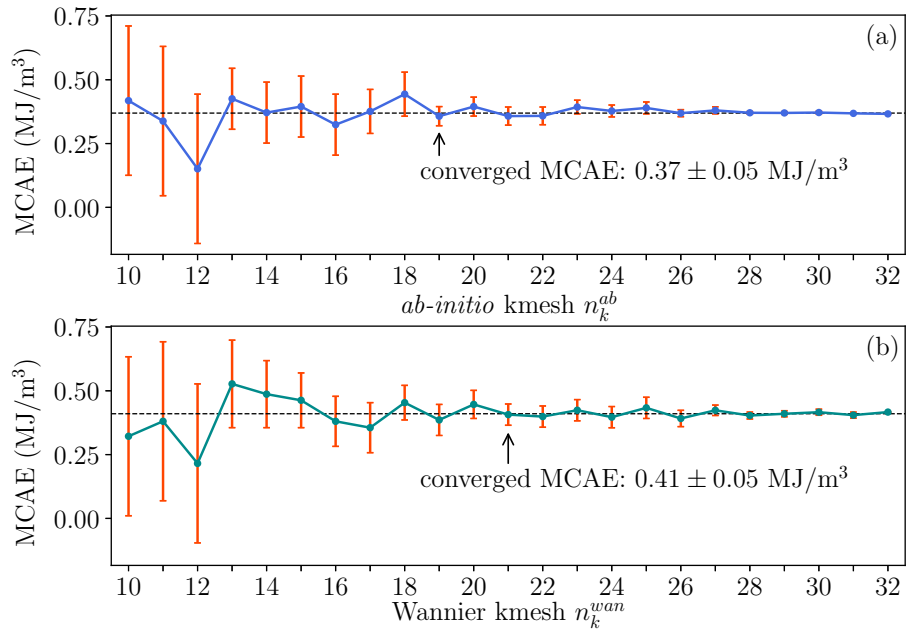
Figure 7: FeNi alloy MCAE convergence relative to (a) *ab-initio* kmesh $n_k^{ab}$, and (b) Wannier interpolation kmesh $n_k^{wan}$. The MLWFs were constructed from *ab-initio* kmesh $12 \times 12 \times 8$, and it is clear from (a) that this kmesh is far from convergence if evaluating MCAE by direct *ab-initio* calculation. In fact, a kmesh of $19 \times 19 \times 13$ is needed for the *ab-initio* calculation to converge. The error bars are the convergence indicators obeying the definition of Equ.(17).

Table 4: The convergence of FeNi alloy MCAE with respect to the *ab-initio* kmesh $n_k^{ab}$, Wannier interpolation kmesh $n_k^{wan}$ and smearing width $\sigma$. The MCAEs in rows of No.1 to 3 are directly calculated by GPAW, while the MCAEs in rows of No.4 to 7 are calculated by Wannier interpolation. The No.8 to 10 rows are the results of VASP[49], WIEN2K[48] and SPR-KKR[48] calculations respectively. The No.11 and 12 rows are the results of experiments[50, 47]. The number $n_k$ in columns 2 and 3 stands for kmesh $n_k \times n_k \times int(\frac{a}{c}n_k)$ where $a$ and $c$ are the in-plane and out-of-plane lattice constants, $int(x)$ means truncating real number $x$ into its integer part, i.e. $n_k \times n_k \times int(\frac{a}{c}n_k)$ means a uniformly distributed kmesh. The $n_k^{ab}$ in rows No.8 to 10 are the total number of $k$-points in the BZ.

| No. | $n_k^{ab}$ | $n_k^{wan}$ | $\sigma$ (eV) | MCAE (MJ/m$^3$) | Notes |
|-----|-----------|-------------|---------------|-----------------|-------|
| 1 | 11 | None | 0.1 | 0.34 | GPAW |
| 2 | 12 | None | 0.1 | 0.15 | GPAW |
| 3 | $\geq$19 | None | 0.1 | $0.37 \pm 0.05$ | GPAW |
| 4 | 10 | $\geq$21 | 0.1 | $0.43 \pm 0.05$ | Wan |
| 5 | 11 | $\geq$22 | 0.1 | $0.54 \pm 0.05$ | Wan |
| 6 | 12 | $\geq$21 | 0.1 | $0.41 \pm 0.05$ | Wan |
| 7 | 12 | $\geq$67 | 0.0 | $0.52 \pm 0.05$ | Wan |
| 8 | 19800 | | | 0.56 | VASP[49] |
| 9 | 20000 | | | 0.48 | WIEN2K[48] |
| 10 | 160000 | | | 0.77 | SPR-KKR[48] |
| 11 | | | | 0.63 | Exp.[50] |
| 12 | | | | 0.58 | Exp.[47] |

the overlap and projection matrices which can be obtained merely from Bloch functions.

First, we take a Fe chain as an example and demonstrate that our Wannier interpolation approach for MCAE achieves a 48 times speedup compared to the direct dense kmesh *ab-initio* calculation, and in this example we discuss three critical factors for successfully getting high accuracy MCAE: the coarse *ab-initio* kmesh for constructing MLWFs, the dense Wannier interpolation kmesh and the smearing width. It is found that the most important issue is the quality of MLWFs, and we need a sufficiently dense kmesh to reach a reliable MCAE, but this kmesh is still much sparser than direct *ab-initio* calculation. The Wannier interpolation kmesh can be easily increased and smearing width can be reduced to 0. Then, the Fe monolayer and the FeNi alloy example demonstrate that our Wannier interpolation approach is capable of calculating MCAE on the order of meV to $\mu$eV, greatly mitigating the computational burden on calculating interface and bulk MCAE. In summary, to get the most accurate MCAE, no smearing should be adopted and the coarse kmesh *ab-initio* calculation should be fully tested. The convergence relative to the Wannier interpolation kmesh can be easily achieved.

The cooperations of QE-Wannier90 and GPAW-Wannier90 demonstrate that the Wannier interpolation approach can work with different *ab-initio* calculators seamlessly. We expect that the Wannier interpolation approach for MCAE can

be more useful when the quality of the interfaces between *ab-initio* calculators and Wannier90 are improved. This Wannier interpolation method reduces the computational cost significantly and maintains high accuracy simultaneously. Besides, it makes it possible for MCAE calculations which are hard to converge or unfeasible due to the computational cost, as well as high-throughput calculations to identify material candidates for spintronics devices.

## Acknowledgments

## References

[1] G. H. O. Daalderop, P. J. Kelly, M. F. H. Schuurmans, First-principles calculation of the magnetocrystalline anisotropy energy of iron, cobalt, and nickel, Phys. Rev. B 41 (1990) 11919. `doi:10.1103/PhysRevB.41.11919`.

[2] P. Bruno, Magnetismus von Festkörpern und grenzflächen, Forschungszentrum Jülich GmbH, 1993, Ch. Physical Origins and Theoretical Models of Magnetic Anisotropy, pp. 24.1–24.28.

[3] J. M. D. Coey, Magnetism and Magnetic Materials, Cambridge University Press, 2010. `doi:10.1017/CBO9780511845000`.

[4] L. Szunyogh, B. Újfalussy, P. Weinberger, Magnetic anisotropy of iron multilayers on Au(001): First-principles calculations in terms of the fully relativistic spin-polarized screened KKR method, Phys. Rev. B 51 (15) (1995) 9552–9559. `doi:10.1103/PhysRevB.51.9552`.

[5] M. Eisenbach, B. L. Györffy, G. M. Stocks, B. Újfalussy, Magnetic anisotropy of monoatomic iron chains embedded in copper, Phys. Rev. B 65 (14) (2002) 144424. `doi:10.1103/PhysRevB.65.144424`.

[6] B. Lazarovits, L. Szunyogh, P. Weinberger, B. Újfalussy, Magnetic properties of finite Fe chains at fcc Cu(001) and Cu(111) surfaces, Phys. Rev. B 68 (2) (2003) 024433. `doi:10.1103/PhysRevB.68.024433`.

[7] S. S. A. Razee, J. B. Staunton, F. J. Pinski, First-principles theory of magnetocrystalline anisotropy of disordered alloys: Application to cobalt platinum, Phys. Rev. B 56 (13) (1997) 8082–8090. `doi:10.1103/PhysRevB.56.8082`.

[8] M. Wang, W. Cai, K. Cao, J. Zhou, J. Wrona, S. Peng, H. Yang, J. Wei, W. Kang, Y. Zhang, J. Langer, B. Ocker, A. Fert, W. Zhao, Current-induced magnetization switching in atom-thick tungsten engineered perpendicular magnetic tunnel junctions with large tunnel magnetoresistance, Nat. Commun. 9 (1) (2018) 671. `doi:10.1038/s41467-018-03140-z`.

[9] S. Peng, W. Zhao, J. Qiao, L. Su, J. Zhou, H. Yang, Q. Zhang, Y. Zhang, C. Grezes, P. K. Amiri, K. L. Wang, Giant interfacial perpendicular magnetic anisotropy in mgo/cofe/capping layer structures, Appl. Phys. Lett. 110 (2017) 072403. `doi:10.1063/1.4976517`.

[10] J. Qiao, S. Peng, Y. Zhang, H. Yang, W. Zhao, First-principles investigation of magnetocrystalline anisotropy oscillations in $co_2FeAl/Ta$ heterostructures, Phys. Rev. B 97 (2018) 054420. `doi:10.1103/PhysRevB.97.054420`.

[11] S. Ouazi, S. Vlaic, S. Rusponi, G. Moulas, P. Buluschek, K. Halleux, S. Bornemann, S. Mankovsky, J. Minár, J. Staunton, *et al.*, Atomic-scale engineering of magnetic anisotropy of nanostructures through interfaces and interlines, Nat. Comm. 3 (2012) 1313. `doi:10.1038/ncomms2316`.

[12] C.-H. Chang, K.-P. Dou, Y.-C. Chen, T.-M. Hong, C.-C. Kaun, Engineering the interlayer exchange coupling in magnetic trilayers, Sci. Rep. 5 (2015) 16844. `doi:10.1038/srep16844`.

[13] C.-H. Chang, K.-P. Dou, G.-Y. Guo, C.-C. Kaun, Quantum-well-induced engineering of magnetocrystalline anisotropy in ferromagnetic films, NPG Asia Mater. 9 (2017) e424. `doi:10.1038/am.2017.148`.

[14] J. Åkerman, Toward a universal memory, Science 308 (2005) 508. `doi:10.1126/science.1110549`.

[15] Z. Wang, L. Zhang, M. Wang, Z. Wang, D. Zhu, Y. Zhang, W. Zhao, High-density nand-like spin transfer torque memory with spin orbit torque erase operation, IEEE Electron Device Lett. 39 (2018) 343. `doi:10.1109/LED.2018.2795039`.

[16] J. Mathon, A. Umerski, Theory of tunneling magnetoresistance of an epitaxial fe/mgo/fe(001) junction, Phys. Rev. B 63 (2001) 220403. `doi:10.1103/PhysRevB.63.220403`.

[17] S. Ikeda, J. Hayakawa, Y. Ashizawa, Y. M. Lee, K. Miura, H. Hasegawa, M. Tsunoda, F. Matsukura, H. Ohno, Tunnel magnetoresistance of 604% at 300k by suppression of ta diffusion in cofebmgocofeb pseudo-spin-valves annealed at high temperature, Appl. Phys. Lett. 93 (2008) 082508. `doi:10.1063/1.2976435`.

[18] J. Zhou, W. Zhao, Y. Wang, S. Peng, J. Qiao, L. Su, L. Zeng, N. Lei, L. Liu, Y. Zhang, A. Bournel, Large influence of capping layers on tunnel magnetoresistance in magnetic tunnel junctions, Appl. Phys. Lett. 109 (2016) 242403. `doi:10.1063/1.4972030`.

[19] G. H. O. Daalderop, P. J. Kelly, M. F. H. Schuurmans, First-principles calculation of the magnetic anisotropy energy of (co)n/(x)mmultilayers, Phys. Rev. B 42 (1990) 7270. `doi:10.1103/PhysRevB.42.7270`.

[20] D.-s. Wang, R. Wu, A. J. Freeman, First-principles theory of surface magnetocrystalline anisotropy and the diatomic-pair mode, Phys. Rev. B 47 (1993) 932. `doi:10.1103/PhysRevB.47.14932`.

[21] D.-s. Wang, R. Wu, A. J. Freeman, State-tracking first-principles determination of magnetocrystalline anisotropy, Phys. Rev. Lett. 70 (1993) 869. `doi:10.1103/physrevlett.70.869`.

[22] P. Błoński, J. Hafner, Density-functional theory of the magnetic anisotropy of nanostructures: an assessment of different approximations, J. Phys.: Condens. Matter 21 (2009) 426001. `doi:10.1088/0953-8984/21/42/426001`.

[23] N. Marzari, A. A. Mostofi, J. R. Yates, I. Souza, D. Vanderbilt, Maximally localized wannier functions: Theory and applications, Rev. Mod. Phys. 84 (2012) 1419. `doi:10.1103/RevModPhys.84.1419`.

[24] N. Marzari, D. Vanderbilt, Maximally-localized wannier functions in perovskites: Cubic batio3, AIP Conf. Proc. 436 (1998) 146. `doi:10.1063/1.56269`.

[25] X. Wang, J. R. Yates, I. Souza, D. Vanderbilt, Ab initio calculation of the anomalous hall conductivity by wannier interpolation, Phys. Rev. B 74 (2006) 195118. `doi:10.1103/PhysRevB.74.195118`.

[26] T. Thonhauser, D. Ceresoli, D. Vanderbilt, R. Resta, Orbital magnetization in periodic insulators, Phys. Rev. Lett. 95 (2005) 137205. `doi:10.1103/PhysRevLett.95.137205`.

[27] S. Poncé, E. R. Margine, C. Verdi, F. Giustino, EPW: Electron–phonon coupling, transport and superconducting properties using maximally localized Wannier functions, Comput. Phys. Comm. 209 (2016) 116. `doi:10.1016/j.cpc.2016.07.028`.

[28] G. Pizzi, D. Volja, B. Kozinsky, M. Fornari, N. Marzari, BoltzWann: A code for the evaluation of thermoelectric and electronic transport properties with a maximally-localized Wannier functions basis, Comput. Phys. Comm. 185 (2014) 422. `doi:10.1016/j.cpc.2013.09.015`.

[29] J. R. Yates, X. Wang, D. Vanderbilt, I. Souza, Spectral and fermi surface properties from wannier interpolation, Phys. Rev. B 75 (2007) 195121. `doi:10.1103/PhysRevB.75.195121`.

[30] G. H. O. Daalderop, P. J. Kelly, M. F. H. Schuurmans, Magnetic anisotropy of a free-standing co monolayer and of multilayers which contain co monolayers, Phys. Rev. B 50 (1994) 9989. `doi:10.1103/PhysRevB.50.9989`.

[31] D. Li, A. Smogunov, C. Barreteau, F. Ducastelle, D. Spanjaard, Magnetocrystalline anisotropy energy of fe(001) and fe(110) slabs and nanoclusters: A detailed local analysis within a tight-binding model, Phys. Rev. B 88 (2013) 214413. `doi:10.1103/PhysRevB.88.214413`.

[32] D. Li, C. Barreteau, M. R. Castell, F. Silly, A. Smogunov, Out- versus in-plane magnetic anisotropy of free fe and co nanocrystals: Tight-binding and first-principles studies, Phys. Rev. B 90 (2014) 205409. `doi:10.1103/PhysRevB.90.205409`.

[33] S. Ayaz Khan, P. Blaha, H. Ebert, J. Minár, O. Šipr, Magnetocrystalline anisotropy of FePt: A detailed view, Phys. Rev. B 94 (14) (2016) 144436. `doi:10.1103/PhysRevB.94.144436`.

[34] X. Wang, D. S. Wang, R. Wu, A. J. Freeman, Validity of the force theorem for magnetocrystalline anisotropy, J. Magn. Magn. Mater. 159 (1996) 337. `doi:10.1016/0304-8853(95)00936-1`.

[35] K. Bairagi, A. Bellec, V. Repain, C. Chacon, Y. Girard, Y. Garreau, J. Lagoute, S. Rousset, R. Breitwieser, Y.-C. Hu, Y. C. Chao, W. W. Pai, D. Li, A. Smogunov, C. Barreteau, Tuning the Magnetic Anisotropy at a Molecule-Metal Interface, Phys. Rev. Lett. 114 (2015) 247203. `doi:10.1103/PhysRevLett.114.247203`.

[36] S. Mizukami, F. Wu, A. Sakuma, J. Walowski, D. Watanabe, T. Kubota, X. Zhang, H. Naganuma, M. Oogane, Y. Ando, T. Miyazaki, Long-lived ultrafast spin precession in manganese alloys films with a large perpendicular magnetic anisotropy, Phys. Rev. Lett. 106 (2011) 117201. `doi:10.1103/PhysRevLett.106.117201`.

[37] A. A. Mostofi, J. R. Yates, Y.-S. Lee, I. Souza, D. Vanderbilt, N. Marzari, wannier90: A tool for obtaining maximally-localised Wannier functions, Comput. Phys. Comm. 178 (2008) 685. `doi:10.1016/j.cpc.2007.11.016`.

[38] A. A. Mostofi, J. R. Yates, G. Pizzi, Y.-S. Lee, I. Souza, D. Vanderbilt, N. Marzari, An updated version of wannier90: A tool for obtaining maximally-localised wannier functions, Comput. Phys. Comm. 185 (2014) 2309. `doi:10.1016/j.cpc.2014.05.003`.

[39] N. Marzari, D. Vanderbilt, Maximally localized generalized wannier functions for composite energy bands, Phys. Rev. B 56 (1997) 12847. `doi:10.1103/PhysRevB.56.12847`.

[40] I. Souza, N. Marzari, D. Vanderbilt, Maximally localized wannier functions for entangled energy bands, Phys. Rev. B 65 (2001) 035109. `doi:10.1103/PhysRevB.65.035109`.

[41] P. Giannozzi, S. Baroni, N. Bonini, M. Calandra, R. Car, C. Cavazzoni, D. Ceresoli, G. L. Chiarotti, M. Cococcioni, I. Dabo, *et al.*, Quantum espresso: a modular and open-source software project for quantum

simulations of materials, J. Phys.: Condens. Matter 21 (2009) 395502. `doi:10.1088/0953-8984/21/39/395502`.

[42] P. Giannozzi, O. Andreussi, T. Brumme, O. Bunau, M. B. Nardelli, M. Calandra, R. Car, C. Cavazzoni, D. Ceresoli, M. Cococcioni, *et al.*, Advanced capabilities for materials modelling with Quantum ESPRESSO, J. Phys.: Condens. Matter 29 (2017) 465901. `doi:10.1088/1361-648X/aa8f79`.

[43] A. D. Corso, Pseudopotentials periodic table: From h to pu, Comput. Mater. Sci. 95 (2014) 337. `doi:10.1016/j.commatsci.2014.07.043`.

[44] N. Marzari, D. Vanderbilt, A. De Vita, M. C. Payne, Thermal contraction and disordering of the al(110) surface, Phys. Rev. Lett. 82 (1999) 3296. `doi:10.1103/PhysRevLett.82.3296`.

[45] J. J. Mortensen, L. B. Hansen, K. W. Jacobsen, Real-space grid implementation of the projector augmented wave method, Phys. Rev. B 71 (2005) 035109. `doi:10.1103/PhysRevB.71.035109`.

[46] J. Enkovaara, C. Rostgaard, J. J. Mortensen, J. Chen, M. Dułak, L. Ferrighi, J. Gavnholt, C. Glinsvad, V. Haikola, H. A. Hansen, H. H. Kristoffersen, M. Kuisma, A. H. Larsen, L. Lehtovaara, M. Ljungberg, O. Lopez-Acevedo, P. G. Moses, J. Ojanen, T. Olsen, V. Petzold, N. A. Romero, J. Stausholm-Møller, M. Strange, G. A. Tritsaris, M. Vanin, M. Walter, B. Hammer, H. Häkkinen, G. K. H. Madsen, R. M. Nieminen, J. K. Nørskov, M. Puska, T. T. Rantala, J. Schiøtz, K. S. Thygesen, K. W. Jacobsen, Electronic structure calculations with GPAW: a real-space implementation of the projector, J. Phys.: Condens. Matter 22 (25) (2010) 253202. `doi:10.1088/0953-8984/22/25/253202`.

[47] M. Mizuguchi, T. Kojima, M. Kotsugi, T. Koganezawa, K. Osaka, K. Takanashi, Artificial Fabrication and Order Parameter Estimation of L10-ordered FeNi Thin Film Grown on a AuNi Buffer Layer, J. Magn. Soc. Jpn. 35 (4) (2011) 370–373. `doi:10.3379/msjmag.1106R008`.

[48] A. Edström, J. Chico, A. Jakobsson, A. Bergman, J. Rusz, Electronic structure and magnetic properties of $L1_0$ binary alloys, Phys. Rev. B 90 (1) (2014) 014402. `doi:10.1103/PhysRevB.90.014402`.

[49] Y. Miura, S. Ozaki, Y. Kuwahara, M. Tsujikawa, K. Abe, M. Shirai, The origin of perpendicular magneto-crystalline anisotropy in L1 0 –FeNi under tetragonal distortion, J. Phys.: Condens. Matter 25 (10) (2013) 106005. `doi:10.1088/0953-8984/25/10/106005`.

[50] T. Shima, M. Okamura, S. Mitani, K. Takanashi, Structure and magnetic properties for L10-ordered FeNi films prepared by alternate monatomic layer deposition, J. Magn. Magn. Mater. 310 (2, Part 3) (2007) 2213–2214. `doi:10.1016/j.jmmm.2006.10.799`.